Numerical simulations of tension tests with a new rate and temperature dependent continuum damage and fracture model

Steffen Gerke, Michael Brünig
Institut für Mechanik und Statik, Universität der Bundeswehr München,
Werner-Heisenberg-Weg 39, D-85577 Neubiberg, Germany

Summary:

The new continuum damage model is based on a general thermodynamic framework for the modeling of rate and temperature dependent behavior of anisotropically damaged elastic-plastic materials subjected to fast deformation. The introduction of damaged and fictitious undamaged configurations allows the definition of damage tensors and the corresponding free energy functions leads to material laws effected by damage and temperature. A generalized hydrostatic-stress-dependent yield condition and a non-associated flow rule describe the plastic material behavior. The damage condition and the corresponding damage rule strongly depend on stress triaxiality. Furthermore the rate and temperature dependence is reflected in a multiplicative decomposition of the plastic hardening and damage softening function. The macro crack behavior is characterized by a triaxiality dependent fracture criteria.

The continuum damage model is implemented into LS-DYNA as user defined material model. Corresponding numerical simulations of unnotched and notched tension tests with high strain rates demonstrate the plastic and damage processes during the deformation leading to final fracture which is numerically predicted by an element erosion technique.

Keywords:

Ductile materials, damage and fracture, stress triaxiality dependence

1 Introduction

Due to rapid simultaneous progress in hardware technologies as well as in computational mechanics and material modeling during the last decades, engineers are nowadays able to analyze complex structures undergoing static and dynamic loading conditions. Consequently, the accurate and realistic modeling of rate-independent and of rate-dependent inelastic behavior of ductile metals is essential for the solution of numerous boundary-value problems occurring in many engineering disciplines. In addition, high strain rate deformations such as dynamic shear banding, impact problems or high-speed machining have become increasingly important for industrial applications. Currently, there are many computer codes for numerical analyses of these problems. Although these codes can nowadays be used to perform computations of structures even under dynamic loading conditions, it is generally agreed that there is a need for improved strength models applicable for a wide range of stress triaxialities as well as corresponding procedures to identify the parameters for these models.

Within the context of dynamic modeling this requires generalized constitutive equations describing the rate-dependent inelastic behavior of metals as functions of strains, strain rates and temperature. For example, due to simplicity many numerical simulations are based on the Johnson-Cook material model [10] accounting for isotropic strain hardening, strain rate sensitivity and thermal softening in an uncoupled form in one single equation. Rohr et al. [12], however, have shown that the Johnson-Cook model might lead to questionable results in the high-dynamic region and, thus, there is a necessity of more reliable and adequate material models.

The objective of the present paper is to discuss a set of constitutive equations for large rate-dependent elastic-plastic-damage materials at elevated temperatures which may be useful for application to the analysis of adiabatic deformation processes for a wide range of stress triaxialities. The rate- and temperature-dependent deformation behavior of anisotropically damaged elastic-plastic materials subjected to impact loading conditions is based on the concepts of continuum damage mechanics. Since the material macroscopic thermomechanical response under large strain and high strain rate deformation loading is governed by different physical mechanisms, a multi-dissipative model is introduced with manifold structure accounting for dislocations along crystal slip planes (plasticity) as well as void and microcrack interactions (damage). It incorporates thermomechanical coupling effects as well as internal dissipative mechanisms through rate-dependent constitutive relations with a set of internal variables. The effect of stress triaxiality on the onset and evolution of plastic flow, damage and failure is discussed. It takes into account a stress-triaxiality dependent yield condition as well as damage and failure criteria with different branches corresponding to various damage and failure modes depending on stress triaxiality. The explicit finite element program LS-DYNA augmented by an user-defined material subroutine is used to perform numerical simulations of dynamic experiments with different specimens. Here good correlation of published experimental data and numerical results is achieved.

2 Continuum Plasticity, Damage and Fracture Model

A macroscopic continuum model is used to predict the irreversible material behavior while ignoring details of the microscopic mechanisms of individual grains and voids as well as their interaction. Brünig [4] proposed a phenomenological framework to describe the inelastic deformations including anisotropic damage by microdefects which has been extended for rate and temperature dependent material behavior [5]. The approach based on the introduction of damaged as well as corresponding fictitious undamaged configurations is also used here and will be briefly summarized in the following.

2.1 Undamaged Configurations

The effective undamaged configurations are considered to formulate the constitutive equations describing the effective elastic-plastic deformation behavior of the undamaged matrix material. Assuming isotropic hyperelasticity the effective stress tensor is expressed in the form

$$\bar{\mathbf{T}} = 2G\mathbf{A}^{\mathrm{el}} + \left(K - \frac{2}{3}G\right) \mathrm{tr}\mathbf{A}^{\mathrm{el}}\mathbf{1} - 3K\alpha_T\left(\theta - \theta_o\right)\mathbf{1}. \tag{1}$$

where G and K represent the shear and bulk modulus of the matrix material, θ the absolute temperature, α_T the coefficient of thermal expension and $\mathbf{A}^{\text{el}}$ is the elastic part of the logarithmic strain tensor.

Furthermore, the rate-dependent plastic behavior of the considered ductile metals is assumed to be governed by the dynamic representation of the Drucker-Prager-type yield condition

$$f^{\text{pl}} = a\bar{I}_1 + \sqrt{\bar{J}_2} - c\left(\gamma, \dot{\gamma}, \theta\right) = 0. \tag{2}$$

In Eq. (2) a represents the hydrostatic stress coefficient while $\bar{I}_1 = \text{tr}\bar{\mathbf{T}}$ is the first invariant of the effectice stress tensor (1) and $\bar{J}_2 = \frac{1}{2}\text{dev}\bar{\mathbf{T}} \cdot \text{dev}\bar{\mathbf{T}}$ denotes the second invariant of the effective stress deviator. In addition, c means the equivalent stress measure expressed as a specific function of plastic strain, plastic strain rate and temperature using the multiplicative decomposition

$$c\left(\gamma, \dot{\gamma}, \theta\right) = \tilde{c}\left(\gamma\right) f_1\left(\dot{\gamma}\right) f_2\left(\theta\right), \tag{3}$$

with the functions

$$\tilde{c}\left(\gamma\right) = \tilde{c}_o \left(\frac{H_o \gamma}{n\tilde{c}_o} + 1\right)^n, \quad f_1\left(\dot{\gamma}\right) = 1 + d\left(\frac{\dot{\gamma} - \dot{\gamma}_o}{\dot{\gamma}_o}\right)^m \quad \text{and} \quad f_2\left(\theta\right) = 1 - b\left(\frac{\theta - \theta_o}{\theta_m}\right)^q. \tag{4}$$

Here the reference equivalent effective stress $\tilde{c}$ can be numerically simulated by the power law where $\tilde{c}_o$ represents the initial yield stress, H_o denotes the initial hardening modulus and n means the hardening exponent. These material parameters are determined performing quasistatic tension tests with smooth specimens leading to homogeneous one-dimensional stress-states at constant reference temperature θ_o. The experimentally observed increasing dependence of the equivalent stress on the inelastic strain rate $\dot{\gamma}$ is described by the strain rate hardening function f_1 with the constitutive parameters d and m which have to be determined by a series of dynamic experiments at different strain rates and constant temperature. The reference inelastic strain rate $\dot{\gamma}_o$ is given by the quasi-static reference tests. In addition, the decrease in equivalent stress with increasing temperature as observed in experiments is taken into account by the thermal softening function f_2 with the constitutive parameters b and q which have to be determined by a series of isothermal tests at different constant temperatures and constant strain rates, whereas θ_m denotes the melting temperature of the matrix material.

In elastic-plastically deformed and damaged metals, irreversible volumetric strains are mainly caused by damage and, in comparison, volumetric plastic strains are negligible. Thus, the isochoric effective plastic strain rate

$$\dot{\bar{\mathbf{H}}}^{\text{pl}} = \dot{\gamma}\frac{1}{\sqrt{2\bar{J}_2}}\text{dev}\bar{\mathbf{T}} \tag{5}$$

describes the evolution of plastic deformations.

In the present paper, only adiabatic processes are considered and, as a consequence, no constitutive equation for the effective heat flux vector is required [5]. The evolution equation for the temperature is approximated by

$$c_F \dot{\theta} = \xi \bar{\mathbf{T}} \cdot \dot{\bar{\mathbf{H}}}^{\text{pl}} \tag{6}$$

only taking into account the inelastic contribution to heating validated by the high-deformation experiments. In Eq. (6) c_F denotes the specific heat and ξ defines the fraction of plastic work rate converted to heating. This latter parameter has been controversely discussed in the literature (see, for example, [8] for further details), and in the present paper it is taken to be constant $\xi = 0.8$.

2.2 Anisotropically damaged configurations

The anisotropically damaged configurations are considered and used to formulate damaged elastic and damage constitutive equations characterizing the inelastic deformation behavior of the damaged aggregate. Experiments reported by Spitzig et al. [13] have shown that the existence of microdefects results in a decrease of the stress level in the aggregate and in a decrease of the elastic material properties when

compared to the response of the virgin undamaged material. Thus, the stress tensor of the damaged ductile solid is given by

$$\mathbf{T} = 2\left(G+\eta_2 \mathrm{tr}\mathbf{A}^{\mathrm{da}}\right)\mathbf{A}^{\mathrm{el}} - 3K\alpha_T\left(\theta-\theta_o\right)\mathbf{1} + \left[\left(K-\frac{2}{3}G+2\eta_1\mathrm{tr}\mathbf{A}^{\mathrm{da}}\right)\mathrm{tr}\mathbf{A}^{\mathrm{el}} + \eta_3\left(\mathbf{A}^{\mathrm{da}}\cdot\mathbf{A}^{\mathrm{el}}\right)\right]\mathbf{1} + \eta_3\mathrm{tr}\mathbf{A}^{\mathrm{el}}\mathbf{A}^{\mathrm{da}} + \eta_4\left(\mathbf{A}^{\mathrm{el}}\mathbf{A}^{\mathrm{da}} + \mathbf{A}^{\mathrm{da}}\mathbf{A}^{\mathrm{el}}\right). \tag{7}$$

where $\eta_1 ... \eta_4$ are material parameters taking into account the deterioration of the elastic properties due to the occurrence of damage [4] and $\mathbf{A}^{\mathrm{da}}$ denotes the damage part of the strain tensor.

In addition, constitutive equations for damage evolution are required and the determination of onset and continuation of damage is based on the concept of damage surface at the macroscopic level formulated in stress space. The model takes into account different damage mechanisms in ductile metals leading to final fracture [1], see Fig. 1. Brünig et al. [6] considering a wide range of stress triaxialities with different branches: damage is characterized by shear modes for negative stress triaxialities $(\eta_c \leq \eta \leq 0)$, by void-growth-dominated modes for large positive triaxialities $(\eta \geq \eta_t)$ and by mixed modes for lower positive stress triaxialities $(0 < \eta < \eta_t)$. In the hydrostatic pressure regime $(\eta < \eta_c)$, Bao and Wierzbicki [2] proposed a cut-off value of stress triaxiality below which damage and fracture do not occur in ductile metals. This stress-triaxiality-dependent concept schematically illustrated in Fig. 1 is also used in the present rate and temperature dependent continuum damage and failure approach.

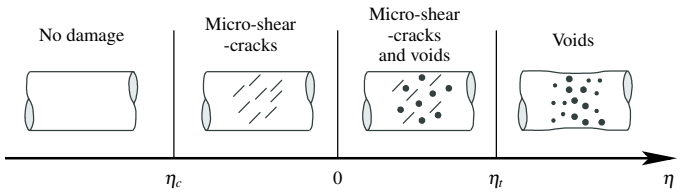

Figure 1: Different damage mechanisms depending on stress triaxiality η

In particular, onset and continuation of damage is characterized by the dynamic damage condition

$$f^{\mathrm{da}}\left(\mathbf{T},\sigma\right) = \tilde{\alpha}I_1 + \tilde{\beta}\sqrt{J_2} - \sigma\left(\mu,\dot{\mu},\theta\right) = 0 \tag{8}$$

expressed in terms of the first stress invariant $I_1 = \mathrm{tr}\mathbf{T}$ and the second invariant of the stress deviator $J_2 = \frac{1}{2}\mathrm{dev}\mathbf{T}\cdot\mathrm{dev}\mathbf{T}$, σ denotes the damage threshold depending on the equivalent damage strain, equivalent damage strain rate and temperature, and the parameters $\tilde{\alpha}$ and $\tilde{\beta}$ describe the influence of stress triaxiality $\eta = I_1/\left(3\sqrt{3J_2}\right)$ on the damage condition:

$$\tilde{\alpha} = \begin{cases} 0 & \text{for} \quad \eta_c \leq \eta \leq 0 \\ 1/3 & \text{for} \quad \eta > 0, \end{cases} \quad \text{and} \quad \tilde{\beta} = \begin{cases} 1 & \text{for} \quad \eta_c \leq \eta \leq 0 \\ 1-\left(\tilde{d}\eta\right)^{\tilde{m}} & \text{for} \quad 0 < \eta < \eta_t \\ 0 & \text{for} \quad \eta \geq \eta_t. \end{cases} \tag{9}$$

In the case of dynamic applications, the equivalent stress is expressed as a specific function of damage accumulation, its rate and temperature using the multiplicative decomposition

$$\sigma\left(\mu,\dot{\mu},\theta\right) = \tilde{\sigma}\left(\mu\right) f_3\left(\dot{\mu}\right) f_2\left(\theta\right). \tag{10}$$

In Eq. (10) the reference stress is numerically simulated by the quadratic relation

$$\tilde{\sigma}\left(\mu\right) = \frac{-\left(\frac{\partial\tilde{c}}{\partial\gamma}\mu_e + \tilde{\sigma}_o\right)}{\mu_e^2}\mu^2 + \frac{\partial\tilde{c}}{\partial\gamma}\mu + \tilde{\sigma}_o \tag{11}$$

shown in Fig. 2 where $\tilde{\sigma}_o$ represents the initial damage strength, μ_e the fictitious value where the damage softening relation reaches zero and $\partial\tilde{c}/\partial\gamma$ the slope of the static plastic hardening function indicated in Eq. (4) at the onset of damage. The equivalent stress (11) is determined using quasistatic tests at

constant temperature θ_o. The experimentally observed increasing dependence of the equivalent stress on the inelastic strain rate $\dot{\mu}$ is described by the damage rate hardening function

$$f_3(\dot{\mu}) = 1 + h\left(\frac{\dot{\mu} - \dot{\mu}_o}{\dot{\mu}_o}\right)^r \tag{12}$$

with the constant parameters h and r obtained from a series of dynamic experiments at different damage rates and constant temperature, and the reference damage rate $\dot{\mu}_o$ is given by the quasi-static reference test.

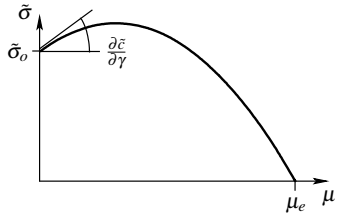

Figure 2: Damage softening law

The damage evolution law models the increase in macroscopic strains caused by the simultaneous growth of voids, their coalescence as well as the evolution of micro-cracks and micro-shearcracks leading to anisotropic damage behavior. This will be adequately described by the damage rule

$$\dot{\mathbf{H}}^{\text{da}} = \dot{\mu}\alpha\mathbf{1} + \dot{\mu}\beta\frac{1}{2\sqrt{J_2}}\text{dev}\mathbf{T} \tag{13}$$

where the first term represents the rate of inelastic volumetric deformations caused by the isotropic growth of voids and the second term corresponds to the anisotropic evolution of damage strain rates caused by micro-shear-cracks.

2.3 Fracture criteria

Moreover, the internal damage variable μ can be used to define a simple triaxiality dependent fracture criterion. This fracture condition can be written in the form

$$f^{\text{cr}} = \mu - \mu_{\text{cr}} = 0 \tag{14}$$

where μ_{cr} is the triaxiality dependent critical equivalent damage strain:

$$\mu_{\text{cr}} = \begin{cases} \mu_f & \text{for} \quad \eta > \eta_f \\ \frac{\mu_f - \mu_o}{\eta_f}\eta + \mu_o & \text{for} \quad 0 \le \eta \le \eta_f \\ \mu_o & \text{for} \quad \eta < 0. \end{cases} \tag{15}$$

and the material parameters μ_f and μ_o represent the critical tension and compression values of the equivalent damage strain. The propagation of the macro crack is numerically realized through an element erosion technique.

3 Numerical examples

The split Hopkinson-Bar method is a well known testing technique to achieve very high strain rates. The experimental setup basically consists of two relatively long bars, called input and output bar in-between which a relatively small specimen is located. At the input bar a wave is generated which causes mayor deformation of the specimen and is partly transmitted to the output bar.

Børvik et al. [3] presented numerical simulations of dynamic tension tests with unnotched and notched axisymmetric specimens. For their numerical simulations the model was roughly reduced and only the specimens were considered which were modeled by four node axisymmetric finite elements. For the numerical studies discussed in the present paper the explicit finite element code LS-DYNA, enhanced by user-defined material subroutine, has been used. Discretization of the specimen is preformed by eight-node brick elements with one integration point. Following the ideas of Børvik et al. [3], only the specimens are concidered and the boundary conditions are described by a dynamic surface impulse, similar to those occurring in split Hopkinson-Bar experiments, while the other end is fixed. With this approach an excess of numerical efforts is avoided and reasonable results can be expected. However, in the future it is desirable to realize simulations of the complete experimental setup to study further effects in more detail.

The material characteristics are taken from the aluminum alloy described in [6], [7] and [8] where the identification of the corresponding material parameters has been discussed in detail.

3.1 Axisymmetric specimen

Hopperstad et al. [9] used axisymmetric unnotched and notched tension specimens in split Hopkinson-Bar apparatus. The testing programme contained notched specimens with notch radii r_n of 0.4, 0.8 and 2.0mm whereas the inclination angle for the specimens with smaller notch radii was chosen to be $\alpha = 15^\circ$, see Fig. 3.

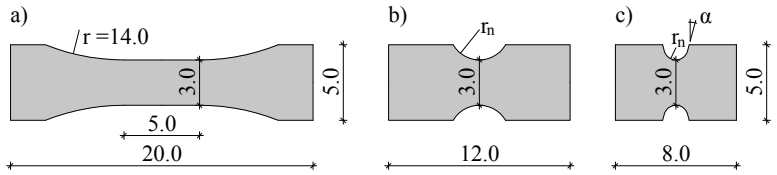

Figure 3: Axisymmetric specimens taken from [9], all dimensions in mm

The corresponding numerical simulations were presented by Børvik et al. [3] who used an axisymmetric finite element model. To avoid numerical costs in the present study the reduced numerical model only considering a part of the specimen as shown in Fig. 3. It is assumed that this approach does not remarkable affect the inelastic deformation behavior and the stress state of the specimen since the material remains elastic in these thicker parts. The simulations are carried out without applying symmetry conditions but Fig. 4 shows for demonstration purposes the mesh of 1/8th of the specimen. For the unnotched and the notched specimen with $r_n = 2.0mm$ a total of 17 elements have been used over the radius leading to a total of 54079 (unnotched) and accordingly 82354 ($r_n = 2.0mm$) elements. For the smaller notch radii of $r_n = 0.8$ and $0.4mm$ 20 elements have been used over the radius which leads to a total of 37789 ($r_n = 0.8mm$) and accordingly 50424 ($r_n = 0.4mm$) elements. Herewith the mesh densities are comparable to those used by [3].

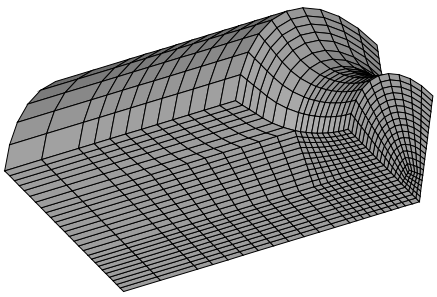

Figure 4: Mesh of 1/8th of notched axisymmetric specimens

Simulations with the unnotched specimen, considering the rate and temperature dependence of the material, show an almost homogeneous evolution of damage over the thinner part although the last image of Fig. 5 shows a very slight necking. Comparing this necking phenomena with the one described in [3] it is remarkable less due to the fact that the here predicted aluminum is less ductile then the Weldox steel used by [9]. A notable necking is numerically predicted if the rate and temperature dependence of the material is neglected in the calculations.

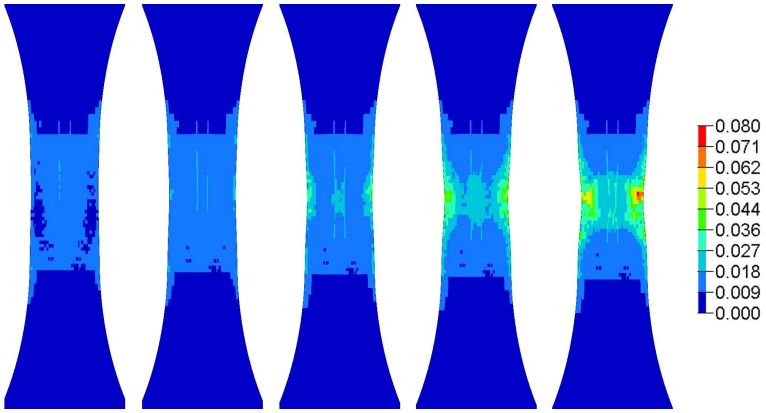

Figure 5: Evolution of damage variable μ for unnotched specimen, first image at $t = 90\mu s$, time in-between images $2.0\mu s$

Fig. 6 displays the triaxiality η, the plastified region at the indicated damage state for the different notch radii 0.4, 0.8 and $2.0mm$. As expected the triaxiality η decreases with increasing notch radius whereas the damaged zone already shows a decreased triaxiality due to damage, i.e. the damaged material reacts softer than the non damaged one. For the biggest notch radius of $r_n = 2.0mm$ the complete notched zone is plastified, which is not the case for the smaller notch radii where the center is not fully plastified at the onset of damage, but with increasing damage zone the center fully plastifies. The onset of damage is for the smallest notch radius of $r_n = 0.4mm$ located at the notch and moves with increasing notch radius towards the center. Comparing the locus of the onset of damage predicted here with the locus of the onset of fracture described by [3] one can notice that they coincide for 0.4 as well as for $2.0mm$ but that [3] indicates the onset of fracture for $r_n = 0.8mm$ also at the center, i.e. where a fully plastified center was obtained.

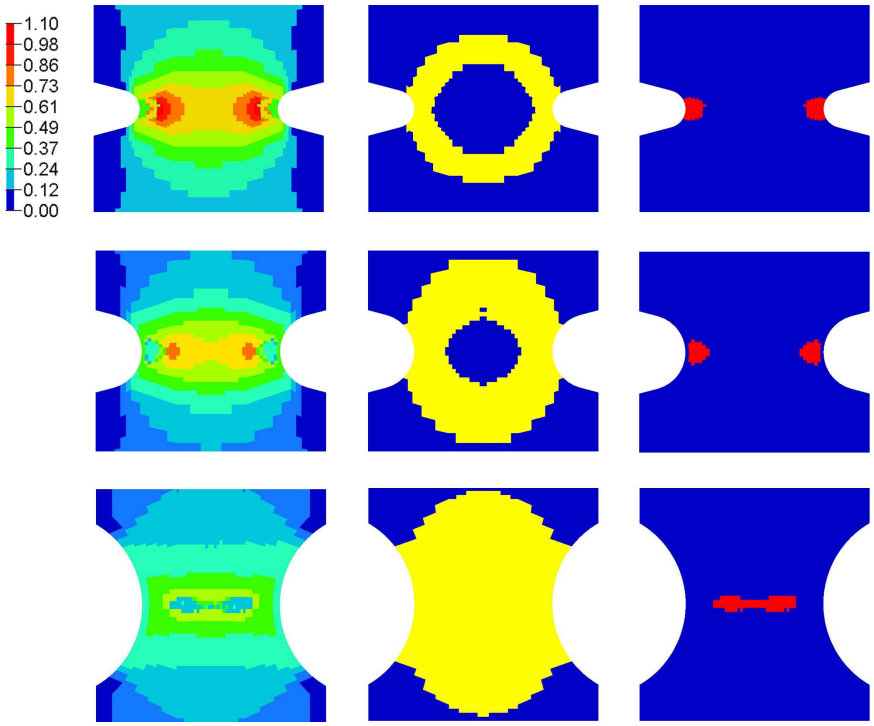

Figure 6: Column: Triaxiality η with corresponding legend, plastic zone at the shown damage state in yellow and damage state in red; row: notch radii 0.4, 0.8 and 2.0mm

Corresponding simulations with rate and temperature independent material behavior, i.e. $f_1 = 1$, $f_2 = 1$ and $f_3 = 1$, have been carried out. The onset of damage is shown in Fig. 7 for the different notch radii. Comparing the locus of the onset of damage with that one obtained for rate and temperature dependent material behavior shown in Fig. 6 it is located more to the center of the specimen.

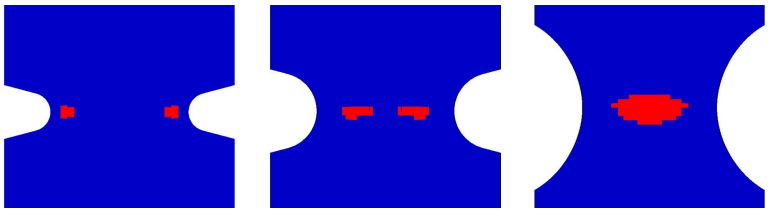

Figure 7: Location of damage occurrence for rate and temperature independent behavior

Applying the fracture criteria described in Eq. (14) to the specimen with $r_n = 0.4mm$ the final fracture surface, shown in Fig. 8, is cup cone shaped, similar to the experimentally obtained one shown in [9].

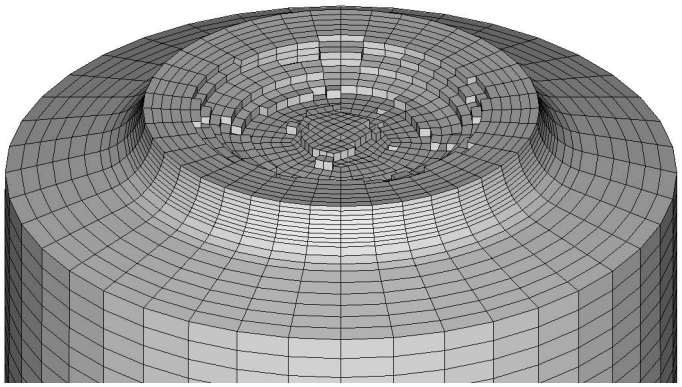

Figure 8: Fracture surface of axisymmetric specimen with $r_n = 0.4mm$

3.2 M-shape specimen

Mohr and Gary [11] proposed a new M-shaped specimen which can be used in split Hopkinson-Bar apparatus to perform tensile experiments. This specimen is specially designed to transform compressive loading conditions into tensile loading in the critical part. The complete specimen is shown in Fig. 9a. Again to avoid extensive numerical costs, the specimen is simplified to only the tension part shown in red. The exact geometry can be seen in Fig. 9b-d. [11] determinated their static material parameters using a 3.5mm thick specimen and dynamic experiments were performed with thicknesses being a multiple of 3.5mm.

This systematic is maintained in the present calculations and first studies with unnotched specimens have been performed with 7.0mm thickness. For better legibility Fig. 10 shows a coarser mesh than used for the simulations with a total of 246528 elements; the thin part of the specimen has 12 elements over the width and 72 elements in thickness direction.

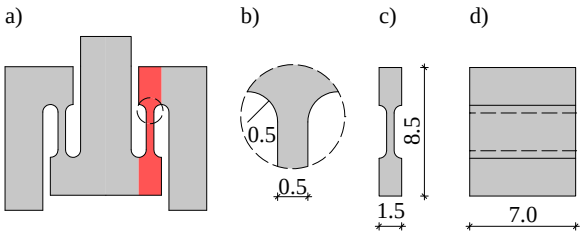

Figure 9: M-shape specimen taken from [11]

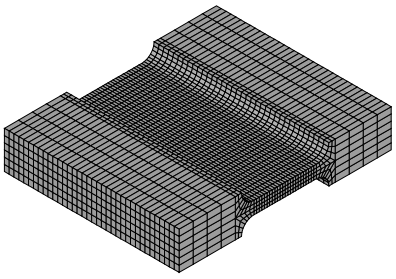

Figure 10: Mesh of M-shape specimen taken from [11]

With the fracture criterion defined in Eq. (14) the complete deformation process, i.e. elastic, elastic-plastic, elastic-plastic-damaged and finally fracture behavior, can be described. Fig. 11 shows the evolution of the internal damage variable μ for rate and temperature dependent material behavior. As

illustrated in the previous examples (Fig. 5) for as well unnotched specimens damage evolutes over the complete thinner part of the specimen over a quite long period of time forming maxima at the center as well as on the edge close to the thicker part of the specimen, see Fig. 11b. Here first fracture occurs almost simultaneously and evolutes from the center horizontally towards the outside and from the edge horizontally towards the center. This causes mayor shear behavior with low positive triaxialities in-between the advancing cracks, see Fig. 12 where the internal damage variable already reached a remarkable value of approximately 4%. In combination with the triaxiality dependence of the fracture criterion this leads to the shown shear fracture. Fig. 13 gives a detailed impression of the fracture surface.

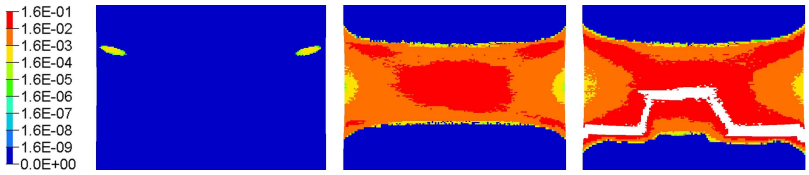

Figure 11: Evolution of internal damage variable μ and fracture for rate and temperature dependent material behavior, thickness 7.0mm, first image at $t = 58\mu s$, time in-between images 6.25μs

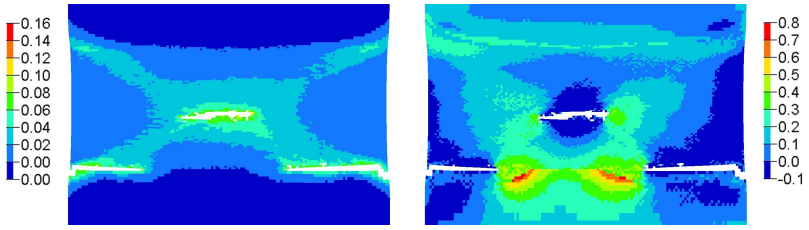

Figure 12: Damage evolution with propagating crack and corresponding triaxiality η distribution

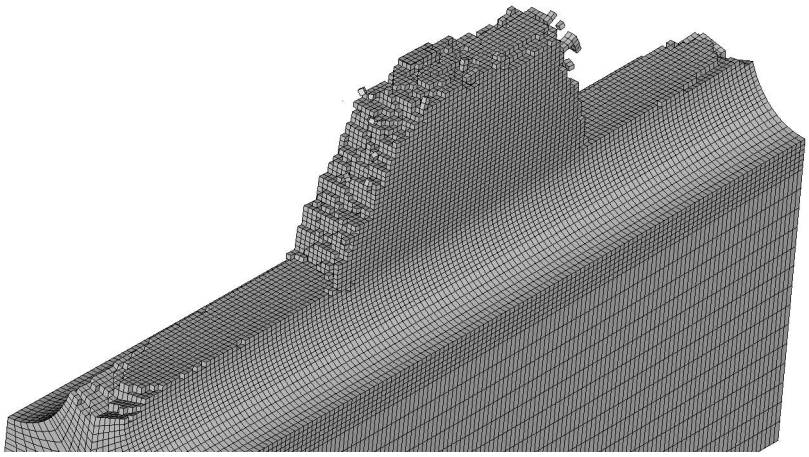

Figure 13: Fracture surface of unnotched specimen with thickness 7.0mm, rate and temperature dependent material behavior

Corresponding simulations with rate and temperature independent material behavior have been performed. The corresponding images of the damage and fracture evolution are shown in Fig. 14. Though the very localized damage evolution after necking the crack starts from the center and evolutes horizontally and the additional damage at the edge, close to the thicker part of the specimen does not effect the final fracture. Thus, rate and temperature effects remarkable affect the fracture process, see Fig. 11 and Fig. 14

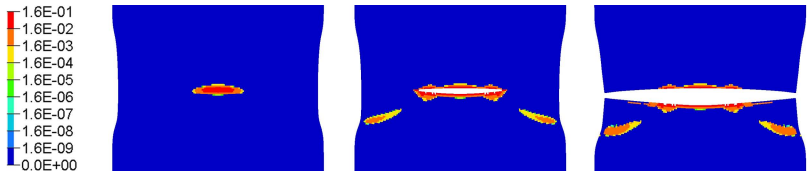

Figure 14: Evolution of internal damage variable μ and fracture for rate and temperature independent material behavior, thickness 7.0mm, first image at $t = 59\mu s$, time in-between first and second image 1.0μs and second and third 3.0μs

4 Conclusions

A rate and temperature dependent continuum damage model has been discussed. The multi-dissipative approach takes into account stress triaxiality dependent plastic flow, damage and failure. The corresponding evolution equations for respective equivalent stress measures are based on multiplicative decomposition of functions simulating equivalent strain, strain rate and temperature effects and has been implemented into the commercial finite element program LS-DYNA as an user-defined material subroutine.

Numerical simulation of Split-Hopkinson-Bar experiments with different specimens have been performed. Evolution of plastic flow, damage, failure and temperature has been discussed for these adiabatic deformation processes. Numerical results have shown good agreement with available experimental data published in the open literature.

5 Literature

[1] Y. Bao and T. Wierzbicki. On the fracture locus in the equivalent strain and stress triaxiality space. *International Journal of Mechanical Sciences*, 46:81–98, 2004.

[2] Y. Bao and T. Wierzbicki. On the cut-off value of negative triaxiality for fracture. *Engineering Fracture Mechanics*, 72:1049–1069, 2005.

[3] T. Børvik, O. S. .Hopperstad, and T. Berstad. On the influence of stress triaxiality and strain rate on the behaviour of a structural steel. part ii. numerical study. *Eur. J. Mech. A/Solids*, 22:15–32, 2003.

[4] M. Brünig. An anisotropic ductile damage model based on irreversible thermodynamics. *Int. J. Plasticity*, 19:1679–1713, 2003.

[5] M. Brünig. Continuum framework for rate-dependent behavior of anisotropic damaged ductile metals. *Acta Mech.*, 186:37–53, 2006.

[6] M. Brünig, D. Albrecht, and S. Gerke. Numerical analyses of stress-triaxiality-dependent inelastic deformation behavior of aluminium alloys. *Int. J. Damage Mech.*, doi:10.1177/1056789509351837, 2009.

[7] M. Brünig, D. Albrecht, and S. Gerke. Modelling of ductile damage and fracture behavior based on different micro-mechanisms. *Int. J. Damage Mech.*, submitted, 2010.

[8] M. Brünig and L. Driemeier. Numerical simulation of taylor impact tests. *International Journal of Plasticity*, 23:1979–2003, 2007.

[9] O. Hopperstad, T. Børvik, M. Langseth, K. Labibes, and C. Albertini. On the influence of stress triaxiality and strain rate on the behaviour of structural steel. part i. experiments. *Eur. J. Mech. A/Solids*, 22:1–13, 2003.

[10] G. R. Johnson and W. H. Cook. A constitutive model and data for metals subjected to large strains, high strain rates and high temperatures. *In: Proceedings of the Seventh International Symposium on Ballistics, Hague, Netherlands*, pages 541–547, 1983.

[11] D. Mohr and G. Gary. M-shaped specimen for the high-strain rate tensile testing using a split hopkinson pressure bar apparatus. *Exp. Mech.*, 47:681–692, 2007.

[12] L. Rohr, H. Nahme, and K. Thoma. Material characterization and constitutive modelling of ductile high strength steel for a wide range of strain rates. *Int. J. Impact Eng.*, 31:401–433, 2005.

[13] W. A. Spitzig, R. E. Smelser, and O. Richmond. The evolution of damage and fracture in iron compacts with various initial porosities. *Acta Metall.*, 36:1201–1211, 1988.

